Available online at www.sciencedirect.com
SCIENCE DIRECT®
International Journal of Heat and Mass Transfer 47 (2004) 1023–1035
International Journal of HEAT and MASS TRANSFER
www.elsevier.com/locate/ijhmt

# Modeling of turbulent opposed-jet mixing flows with $\tilde{\kappa}$–$\tilde{\epsilon}$ model and second-order closure

C.-P. Chou [a,*], J.-Y. Chen [a], J. Janicka [b], E. Mastorakos [c]

[a] Department of Mechanical Engineering, University of California, Berkeley, CA 94720, USA
[b] Fachgebiet für Energie- und Kraftwerkstechnik, Technische Universität Darmstadt, Darmstadt, Germany
[c] Department of Engineering, University of Cambridge, Cambridge, UK

Received 2 July 2002; received in revised form 1 August 2003

**Abstract**

A numerical model for turbulent opposed-jet mixing flows is developed with a one-dimensional (1-D) formulation with various turbulence models. Calculations with different combinations of turbulence and scalar models are conducted. The performances of various models are evaluated by extensive comparisons with existing experimental data. The numerical model is then used for studying the dependence of predicted scalar field on exit bulk velocity and turbulence intensity. Model results in general agree well with trends observed experimentally. The importance of non-zero velocity gradient at jet exit on the predicted results is illustrated through exploration runs. The distribution of mechanical-to-scalar time scale ratio, $C_D$, is deduced from results obtained with a Reynolds stress model. The value of $C_D$ is found to deviate substantially from the commonly used value of 2, especially when the density variation is large.


*Keywords:* Opposed-jet flow; Turbulent scalar mixing; $\tilde{\kappa}$–$\tilde{\epsilon}$; Reynolds stress

## 1. Introduction

Due to its simplicity in geometry, the opposed-jet flow configuration has been used extensively in the past for studying laminar flames [1–3]. Recently, there has been an increasing interest on turbulent combustion with the same configuration. The turbulence is usually generated by a perforated plate upstream of the jet exit. By changing the location of the perforated plate or the number/size of the holes, different levels of turbulence can be achieved [4–6]. Hence the turbulence strain rate can be adjusted independently of mean flow field. The influences of the mean and the turbulent strain rates on flame behaviors ranging from equilibrium to extinction can be studied separately without major modifications to the test rig. From the perspective of theoretical analysis, the advantages associated with the opposed-jet flow configuration are significant. The similarity of velocity near the centerline permits the transformation of the axisymmetric (2-D) partial differential equations to one-dimensional (1-D) ordinary differential equations (ODEs), thus greatly reduces the demand on computer resources. Recently, this 1-D formulation has been validated numerically by Chou et al. [7].

In the past, there have been several numerical and theoretical studies of turbulent opposed-jet flames [8–17]. These studies involved both premixed and non-premixed flames with various types of turbulence and scalar models. In general, the predicted mean axial velocity and mean mixing field were found in reasonable agreement with data reported in the literature. However, the predicted second moments were less satisfactory. For instance, the standard $\tilde{\kappa}$–$\tilde{\epsilon}$ model was found to yield negative normal Reynolds stress components when density change is large [8]. A modified $\tilde{\kappa}$–$\tilde{\epsilon}$ model was introduced by Bray et al. [8] to correct this and this

* Corresponding author. Address: Reaction Design, 6440 Lusk Blvd. D-209, San Diego, CA 92121, USA. Tel.: +1-858-550-1920x28.
*E-mail address:* cpchou@reactiondesign.com (C.-P. Chou).

0017-9310/$ - see front matter © 2003 Elsevier Ltd. All rights reserved.
doi:10.1016/j.ijheatmasstransfer.2003.09.005

**Nomenclature**

$C_\chi$, $C_{d1}$, $C_{d2}$, $C_{d3}$, $C_{d4}$ empirical constants for the scalar dissipation rate equation
$C_{\mathrm{D}}$ mechanical-to-scalar time scale ratio
$C_{ff}$ ($=0.22$) empirical constant for the scalar variance equatio
$C_q$ the normalized turbulent kinetic energy, $C_q \equiv \sqrt{(\widetilde{u''^2} + 2\widetilde{v''^2})/3}/u_0$
$C_s$ empirical constants for the Reynolds stress equations
$C_{sf}$, $C_{f1}$, $C_{f2}$ empirical constants for the $\widetilde{u''f''}$ transport equation
$D_{\mathrm{m}}$ mean molecular diffusion coefficient
$f$ mixture fraction
$G$ $\mathrm{d}U/\mathrm{d}z$
$H$ mean radial pressure gradient
$h$ the spacing between the jet exits
$L_{\mathrm{t}}$ characteristic turbulence length scale
$S_{\mathrm{b}}$ mean strain rate
$p$ pressure
$Re_{\mathrm{t}}$ turbulent Reynolds number
$r$ radial coordinate
$r_\rho$ density ratio of the jet streams
$U$ $\bar{\rho}\tilde{u}/2$
$u$ axial velocity
$v$ radial velocity
$w$ azimuthal velocity
$z$ axial coordinate
$z^*$ normalized axial coordinate, $z^* \equiv 2z/h - 1$

*Greek symbols*
$\chi$ scalar dissipation rate, $\tilde{\chi} \equiv 2D_{\mathrm{m}}\widetilde{\frac{\partial f}{\partial x_j}}\widetilde{\frac{\partial f}{\partial x_j}}$
$\epsilon$ turbulent energy dissipation rate
$\kappa$ turbulent kinetic energy
$\nu$ kinematic viscosity coefficient
$\nu_{\mathrm{t}}$ turbulent kinematic viscosity
$\rho$ mass density
$\sigma_f$, $\sigma_\kappa$, $\sigma_\epsilon$ empirical coefficients in turbulent transport term
$\tau_{\mathrm{f}}$ flow residence time
$\tau_{\mathrm{t}}$ large-eddy turnover time
$\tau_{uu}$, $\tau_{vv}$, $\tau_{ww}$, $\tau_{uv}$ Reynolds stress components
$\xi_f$ reciprocal of mixing time scale

*Superscripts*
— conventional time average
$\sim$ density weighted average (Favre average)
$''$ fluctuation with respect to the Favre average

*Subscripts*
0 air (cold) stream
1 fuel (hot) stream

modification was adopted later by Maury and Libby [12] in modeling of an opposed-jet non-premixed flame. The computed $\tilde{\kappa}$ profile showed a sharp dip at the stagnation plane in disagreement with data which in fact reaches its peak value. The predicted scalar variance was found in poor agreement with the data. Studies using Reynolds stress models were performed by solving modeled transport equations for both the scalar variance and the scalar flux. The scalar dissipation rate was modeled by a fixed mechanical-to-scalar time scale ratio [11,13,14,16]. These studies showed that Reynolds stress models improved the predictions of mean velocities and turbulence intensities in comparison with the $\tilde{\kappa}$–$\tilde{\epsilon}$ model.

As various types of turbulence and scalar models were used in modeling of different types of flames, it is difficult to gauge the merits of different turbulence and scalar models. In addition, models for the interactions between turbulence and chemistry play a critical role in the predictions. A systematic study of numerical models for predictions of mixing field in opposed-jet flows is reported here as the first step toward a comprehensive study of turbulent combustion. This paper is organized as follows. We first report detailed equations for the opposed-jet flows under the one-dimensional formulation. Turbulence closure is provided by the standard $\tilde{\kappa}$–$\tilde{\epsilon}$ model [18] and two versions of second-order closure: one proposed by Launder et al. (LRR) [19] and the other by Speziale et al. (SSG) [20]. Next, two different scalar field models are described including the gradient model and a second-order closure with a modeled transport equation for the scalar dissipation rate. The performances of various turbulence and scalar models are assessed by comparisons with existing experimental data. Through an exploration run, the importance of assigning a non-zero velocity gradient boundary condition at the jet exits is illustrated. Using results obtained from a second-order scalar model, we deduce the distribution of the mechanical-to-scalar time scale ratio, $C_{\mathrm{D}}$. The validity of commonly assumed constant value of $C_{\mathrm{D}}$ for modeling the scalar dissipation rate is examined. The main findings are summarized in the conclusion section.

## 2. Opposed-jet turbulent jet flows

A schematic of an opposed-jet flow is sketched in Fig. 1. Two opposed, axisymmetric jets are directed toward each other with a distance, $h$, which is of the order of jet diameter in most experiments. Studies of mixing can be carried out with fuel in one stream and oxidizer in the

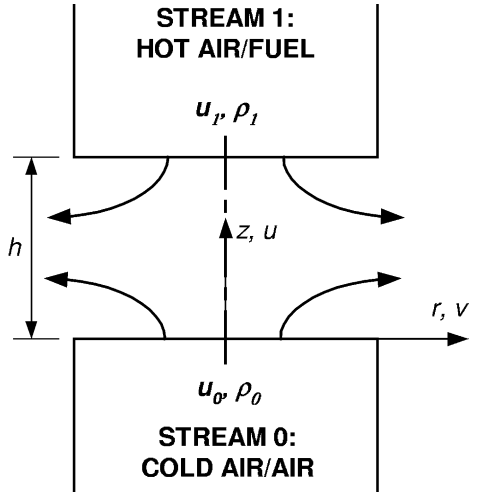


Fig. 1. Schematic of opposed-jet flow configuration.

other stream. Alternatively, air streams at different temperatures can be used. A detailed description of the opposed-jet flow experiments can be found in Ref. [4]. The mean strain rate of the opposed-jet flow is defined as [21]

$$S_b = \frac{u_0}{h}\left(1 + \frac{u_1}{u_0}\sqrt{\frac{\rho_1}{\rho_0}}\right). \tag{1}$$

For opposed jets with equal momentum, Eq. (1) reduces to $S_b = 2u_0/h$, which is referred to as the stagnation-flow velocity gradient [2,21].

### 2.1. Mathematical formulation

With the axisymmetric assumption, the Favre (density weighted) averaged continuity and momentum equations for high-Reynolds number turbulent flows can be written as

Mean continuity equation:

$$\frac{\partial}{\partial z}(\bar{\rho}\tilde{u}) + \frac{1}{r}\frac{\partial}{\partial r}(r\bar{\rho}\tilde{v}) = 0. \tag{2}$$

Mean axial momentum equation:

$$\bar{\rho}\tilde{u}\frac{\partial \tilde{u}}{\partial z} + \bar{\rho}\tilde{v}\frac{\partial \tilde{u}}{\partial r} = -\frac{\partial \bar{p}}{\partial z} - \frac{\partial}{\partial z}\left(\bar{\rho}\widetilde{u''u''}\right) - \frac{\partial}{\partial r}\left(\bar{\rho}\widetilde{u''v''}\right) - \frac{\bar{\rho}\widetilde{u''v''}}{r}. \tag{3}$$

Mean radial momentum equation:

$$\bar{\rho}\tilde{u}\frac{\partial \tilde{v}}{\partial z} + \bar{\rho}\tilde{v}\frac{\partial \tilde{v}}{\partial r} = -\frac{\partial \bar{p}}{\partial r} - \frac{\partial}{\partial z}\left(\bar{\rho}\widetilde{u''v''}\right) - \frac{\partial}{\partial r}\left(\bar{\rho}\widetilde{v''v''}\right). \tag{4}$$

By adopting the approach taken by Kee et al. [2], Eqs. (2)–(4) can be reduced to a one-dimensional boundary-value problem along the centerline. The mean statistics, such as the mean axial velocity, density and other quantities, are assumed functions of axial distance. By introducing two new variables $U(z) \equiv \bar{\rho}\tilde{u}/2$ and $G(z) \equiv \mathrm{d}U(z)/\mathrm{d}z$, the radial velocity can be deduced from continuity equation as $\tilde{v} = -G(z)r/\bar{\rho}$. All the normal stresses are assumed to be functions of $z$ only as $\widetilde{u''u''} = \tau_{uu}(z)$, $\widetilde{v''v''} = \tau_{vv}(z)$, and $\widetilde{w''w''} = \tau_{ww}(z)$. With these, the axial and radial momentum equations are reduced to

$$4U\frac{\mathrm{d}}{\mathrm{d}z}\left(\frac{U}{\bar{\rho}}\right) + \frac{\partial \bar{p}}{\partial z} + \frac{\mathrm{d}}{\mathrm{d}z}(\bar{\rho}\tau_{uu}) + 2\bar{\rho}\tau_{uv} = 0, \tag{5}$$

and

$$-2U\frac{\mathrm{d}}{\mathrm{d}z}\left(\frac{G}{\bar{\rho}}\right) + \frac{G^2}{\bar{\rho}} + H + \frac{\mathrm{d}}{\mathrm{d}z}(\bar{\rho}\tau_{uv}) = 0, \tag{6}$$

where $H(\equiv (1/r)(\partial \bar{p}/\partial r))$ serves as an eigenvalue of the problem. The boundary conditions are: $U(0) = \rho_0 u_0/2$ and $U(h) = \rho_1 u_1/2$. In addition, the axial velocity gradients at the exits need to be specified and will be described in a later section.

### 2.2. Turbulence closure

Three different turbulence models are considered: the standard $\tilde{\kappa}$–$\tilde{\epsilon}$ eddy-viscosity model and two Reynolds stress models proposed by Launder et al. (denoted by RSM-LRR) [19] and by Speziale et al. (denoted by RSM-SSG) [20]. Although the standard $\tilde{\kappa}$–$\tilde{\epsilon}$ model is widely used in modeling of turbulent flows, its applications to opposed-jet flows have been questioned [22,23]. In opposed-jet flows, turbulence components are highly anisotropic due to strong compression of turbulence. This feature is not well treated by the $\tilde{\kappa}$–$\tilde{\epsilon}$ model as it assumes isotropic turbulence. As such, the standard $\tilde{\kappa}$–$\tilde{\epsilon}$ model could yield negative values of turbulence kinetic energy for the radial component [8]. Durbin [24] suggested that the appropriate velocity scale for turbulent transport near the wall is the fluctuating velocity normal to the wall, $\overline{v^2}$ and proposed the $\kappa$–$\epsilon$–$v^2$ model as an improvement to the standard $\tilde{\kappa}$–$\tilde{\epsilon}$ model for wall-bounded flows. The anisotropy of turbulent transport is introduced in the $\kappa$–$\epsilon$–$v^2$ model by using $\overline{v^2}$ as the velocity scale in eddy-viscosity evaluation. An additional transport equation for $\overline{v^2}$ is therefore required and is solved together with the $\kappa$ and $\epsilon$ equations. Note that $\overline{v^2}$ of the $\kappa$–$\epsilon$–$v^2$ model is equivalent to the axial component of turbulent kinetic energy, i.e., $\widetilde{u''^2}$, in opposed-jet flows. Both the Reynolds stress and $\kappa$–$\epsilon$–$v^2$ models are considered better suited for the opposed-jet flows as the anisotropy aspect is included. Because of the simplicity of the current 1-D model, the higher order Reynolds stress models are implemented. For two- or three-dimensional simulations, however, the $\kappa$–$\epsilon$–$v^2$ model may be favorable due to its low computing cost. Detailed

equations for the Reynolds stress closure considered here are described in Appendix A.

### 2.3. Scalar field models

With the equal diffusivity assumption, the mixing field can be described by the mixture fraction as

$$2U\frac{\mathrm{d}\tilde{f}}{\mathrm{d}z} = -\frac{\mathrm{d}}{\mathrm{d}z}\left(\bar{\rho}\widetilde{u''f''}\right). \tag{7}$$

Modeling of the turbulent scalar flux, $\widetilde{u''f''}$, is needed to close Eq. (7). Conventionally, the gradient diffusion model is used with the $\tilde{\kappa}$–$\tilde{\epsilon}$ model and it is expressed as

$$\widetilde{u''f''} = -\frac{\nu_t}{\sigma_f}\frac{\mathrm{d}\tilde{f}}{\mathrm{d}z} \tag{8}$$

with $\sigma_f = 0.7$ [18]. For the Reynolds stress closure, a transport equation for $\widetilde{u''f''}$ is solved with modeling constants taken from [25]

$$\begin{aligned}2U\frac{\mathrm{d}\widetilde{u''f''}}{\mathrm{d}z} &= 2\frac{\mathrm{d}}{\mathrm{d}z}\left(\bar{\rho}C_{sf}\tau_{uu}\frac{\tilde{\kappa}}{\tilde{\epsilon}}\frac{\mathrm{d}\widetilde{u''f''}}{\mathrm{d}z}\right) + \bar{\rho}C_{sf}\tau_{uv}\frac{\tilde{\kappa}}{\tilde{\epsilon}}\frac{\mathrm{d}\widetilde{u''f''}}{\mathrm{d}z}\\ &\quad - \bar{\rho}\left[\tau_{uu}\frac{\mathrm{d}\tilde{f}}{\mathrm{d}z} + 2\widetilde{u''f''}\frac{\mathrm{d}}{\mathrm{d}z}\left(\frac{U}{\bar{\rho}}\right)\right]\\ &\quad - C_{f1}\bar{\rho}\frac{\tilde{\epsilon}}{\tilde{\kappa}}\widetilde{u''f''} + 2C_{f2}\bar{\rho}\left[\widetilde{u''f''}\frac{\mathrm{d}}{\mathrm{d}z}\left(\frac{U}{\bar{\rho}}\right)\right],\end{aligned} \tag{9}$$

where $C_{sf} = 0.35$, $C_{f1} = 2.15$, and $C_{f2} = 0.8$. The variance of the mixture fraction, $\widetilde{f''^2}$, is modeled by [26]

$$\begin{aligned}2U\frac{\mathrm{d}\widetilde{f''^2}}{\mathrm{d}z} &= \frac{\mathrm{d}}{\mathrm{d}z}\left(\bar{\rho}C_{ff}\tau_{uu}\frac{\tilde{\kappa}}{\tilde{\epsilon}}\frac{\mathrm{d}\widetilde{f''^2}}{\mathrm{d}z}\right) + \bar{\rho}C_{ff}\tau_{uv}\frac{\tilde{\kappa}}{\tilde{\epsilon}}\frac{\mathrm{d}\widetilde{f''^2}}{\mathrm{d}z}\\ &\quad - 2\bar{\rho}\widetilde{u''f''}\frac{\mathrm{d}\tilde{f}}{\mathrm{d}z} - \bar{\rho}\tilde{\chi}.\end{aligned} \tag{10}$$

Modeling of the scalar dissipation rate is often done by assuming a constant ratio between the scalar mixing time scale and the turbulence time scale. We use this model with the $\tilde{\kappa}$–$\tilde{\epsilon}$ closure and the scalar dissipation rate is modeled as

$$\tilde{\chi} = C_{\mathrm{D}}\frac{\tilde{\epsilon}}{\tilde{\kappa}}\widetilde{f''^2}, \tag{11}$$

where $C_{\mathrm{D}} = 2$ [27]. However, this practice is not well supported by experimental observations. From the heated grid turbulence experiments, Warhaft and Lumley [28] found the values of $C_{\mathrm{D}}$ ranging from 0.6 to 2.4. Eswaran and Pope [29] performed direct numerical simulations of decaying scalar fields in stationary, homogeneous turbulence. The value of $C_{\mathrm{D}}$ is found higher than 2 when the flow residence time is short (less than 2–3 units of the large-eddy turnover time).

Alternatively, the scalar dissipation rate can be computed by its modeled transport equation (e.g., [25,30]). We use the model proposed by Jones and Musonge [26] and solve for the ratio between $\tilde{\chi}$ and $\widetilde{f''^2}$ for numerical stability. The modeled $\tilde{\chi}$ equation is expressed in terms of $\xi_f(\equiv \tilde{\chi}/\widetilde{f''^2})$ as

$$\begin{aligned}2U\frac{\mathrm{d}\xi_f}{\mathrm{d}z} &= \frac{\mathrm{d}}{\mathrm{d}z}\left(\bar{\rho}C_{\chi}\tau_{uu}\frac{\tilde{\kappa}}{\tilde{\epsilon}}\frac{\mathrm{d}\xi_f}{\mathrm{d}z}\right) + \bar{\rho}C_{\chi}\tau_{uv}\frac{\tilde{\kappa}}{\tilde{\epsilon}}\frac{\mathrm{d}\xi_f}{\mathrm{d}z}\\ &\quad - C_{d1}\bar{\rho}\xi_f^2 - C_{d2}\bar{\rho}\xi_f\frac{\tilde{\epsilon}}{\tilde{\kappa}} - C_{d3}\bar{\rho}\xi_f\frac{\widetilde{u''f''}}{\widetilde{f''^2}}\frac{\mathrm{d}\tilde{f}}{\mathrm{d}z}\\ &\quad - C_{d4}\bar{\rho}\frac{\xi_f}{\tilde{\kappa}}\left[2\tau_{uu}\frac{\mathrm{d}}{\mathrm{d}z}\left(\frac{U}{\bar{\rho}}\right) - \tau_{vv}\frac{G}{\bar{\rho}}\right]\end{aligned} \tag{12}$$

with $C_{\chi} = 0.35$, $C_{d1} = 2.2$, $C_{d2} = 0.9$, $C_{d3} = 1.0$, and $C_{d4} = 1.4$. The boundary conditions for the mean scalar field are $\tilde{f}(0) = 0$ and $\tilde{f}(h) = 1$. All second moments are assigned zero at the jet exits.

## 3. Results and discussion

The effects of various parameters on the computed characteristics of turbulent opposed-jet flows are explored by using various turbulence models. Table 1 lists the flow conditions of opposed-jet flows considered here. The first six conditions correspond to mixing of air streams at different temperatures (difference less than 80 °C). The last one is for air–helium mixing. The first four cases, designated as Cases A through D, correspond to the experiments by Mastorakos [31]. These cases were designed to study the influence of bulk velocity and normalized turbulence intensity $\left(C_q \equiv \sqrt{(\widetilde{u''^2} + 2\widetilde{v''^2})/3}/u_0\right)$ on the flow and mixing fields. Both Case A and Case B have the same level of exit turbulence intensity but Case A has a higher bulk velocity than that of Case B. Cases C and D have the same bulk velocities as those of Cases A and B respectively but with a lower level of exit turbulence intensity.

The next two cases, Cases E and F, correspond to the experiments studied by Sardi et al. [32]. These two cases have the same level of exit turbulence intensity but the bulk velocity of Case F is higher. It is noted that the exit turbulence intensity of Cases E and F are higher than those in Cases A–D. The impact of jet density ratio, $r_\rho$, on the mixing is explored by Case G. The sensitivity of numerical solutions to the non-zero axial velocity gradients is examined by repeating Case B with various boundary conditions.

### 3.1. Effect of bulk velocity

Experimental results by both Mastorakos [31] and Sardi et al. [32] concluded that the flow field of opposed jets can be described by the similarity profiles with the exit velocity being the velocity scale and the jet spacing

Table 1
Flow conditions of mixing in turbulent opposed-jet flows

| | Case | | | | | | |
|---|---|---|---|---|---|---|---|
| | A | B | C | D | E | F | G |
| $u_0$ (cm/s) | 313 | 148 | 313 | 148 | 384 | 544 | 148 |
| $u_1$ (cm/s) | 343 | 162 | 343 | 162 | 400 | 570 | 395 |
| $h$ (cm) | 2.0 | 2.0 | 2.0 | 2.0 | 3.0 | 3.0 | 2.0 |
| $C_q$ | 0.085 | 0.085 | 0.045 | 0.045 | 0.100 | 0.100 | 0.085 |
| $L_{t,0}$ (cm) | 0.40 | 0.40 | 0.40 | 0.40 | 0.28 | 0.28 | 0.40 |
| $Re_t$ | 70 | 33 | 37 | 17 | 73 | 102 | 33 |
| $\tau_f = \frac{h}{2u_0}$ (ms) | 3.2 | 6.8 | 3.2 | 6.8 | 3.8 | 2.6 | 6.8 |
| $\tau_t = \frac{L_{t,0}}{\widetilde{u''}}$ (ms) | 14.9 | 32.3 | 28.6 | 58.8 | 7.2 | 5.1 | 32.3 |
| $\tau_f/\tau_t$ | 0.215 | 0.211 | 0.112 | 0.116 | 0.528 | 0.510 | 0.211 |
| $\rho_1/\rho_0$ | 0.83 | 0.83 | 0.83 | 0.83 | 0.92 | 0.92 | 0.14 |
| Ref. | [4] | [4] | [4] | [4] | [32] | [32] | [–] |

being the length scale. For now, calculations are carried out with zero axial velocity gradient at jet nozzle exits, i.e., $du/dz = 0$. Fig. 2 compares the mean axial velocity profiles of Cases A and B versus the non-dimensional axial distance, $z^*$, defined as $z^* = 2z/h - 1$. Both the experimental data and numerical results confirm that the normalized mean velocity profiles of Cases A and B are similar. Some discrepancies are noted between the model predictions and the data. This will be discussed in the exploration section of boundary conditions for axial velocity gradient.

The normalized root mean square (rms) values of the velocity fluctuations for Cases A and B are compared in Fig. 3. The experimental data exhibit a gradual increase of $\widetilde{u''}$ as the flow approaches the stagnation plane. The peak is located at the stagnation plane and its value is

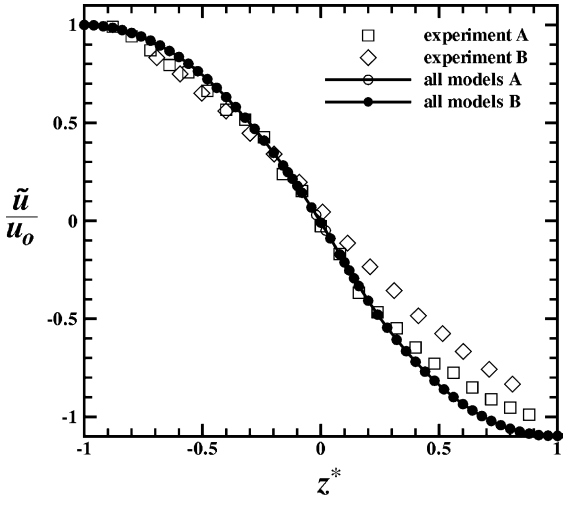


Fig. 2. Normalized mean axial velocity predicted by various 1-D models showing no dependence on turbulence model or bulk velocity.

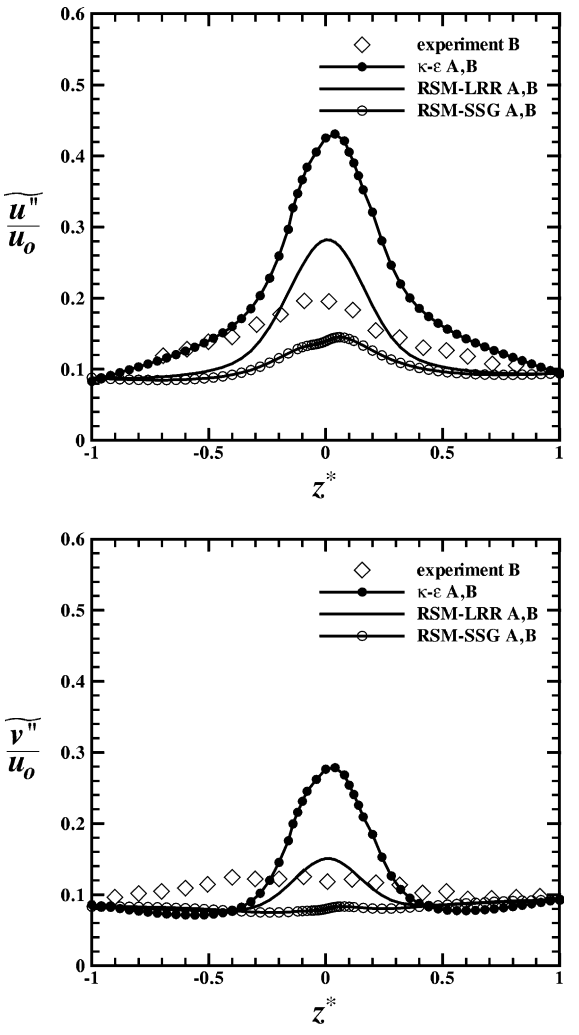


Fig. 3. Comparisons of velocity fluctuation profiles showing a strong anisotropy. Top: axial component; bottom: radial component; experimental data: Mastorakos [4].

about twice of the initial level at the jet exits. Consistent with previous results from the literature [22,23], the $\tilde{\kappa}$–$\tilde{\epsilon}$ model over-predicts the production of $\widetilde{u''}$ leading to a sharp increase of $\widetilde{u''}$ near the stagnation plane. The results of Reynolds stress models, denoted by RSM-LRR and RSM-SSG, agree better with the data than the $\tilde{\kappa}$–$\tilde{\epsilon}$ model. The RSM-LRR model under-predicts the $\widetilde{u''}$ values near the jet exits but over-predicts the peak value by about 50%. The predicted profile of $\widetilde{u''}$ by the RSM-SSG model is seen closely resembling to the data although the peak $\widetilde{u''}$ value is under-predicted by about 30%. The lower plot shows the radial velocity fluctuation, $\widetilde{v''}/u_0$, with its peak value only half of that of $\widetilde{u''}$ revealing that the turbulence is highly anisotropic. The $\tilde{\kappa}$–$\tilde{\epsilon}$ model over-predicts the peak value by a factor of 3. The RSM-LRR model under-predicts the $\widetilde{v''}$ level in regions near the cold jet side (from $z^* = -1$ to $z^* = -0.2$) but gives a peak value within 10% of the experimental value. The RSM-SSG model predicts a nearly flat profile. Among the three models, the predictions by the RSM-LRR model show overall the best agreement with the data.

Fig. 4 compares the mean mixture fraction profiles of Cases A, B, E and F. The predictions by the $\tilde{\kappa}$–$\tilde{\epsilon}$ model are seen in good agreement with the data. The mixing layers predicted by the RSM-LRR model are slightly narrower than the data. The RSM-SSG model yields the least satisfactory results with a very narrow mixing layer which is due to the predicted low turbulence as seen in Fig. 3. Again both the data and model results confirm

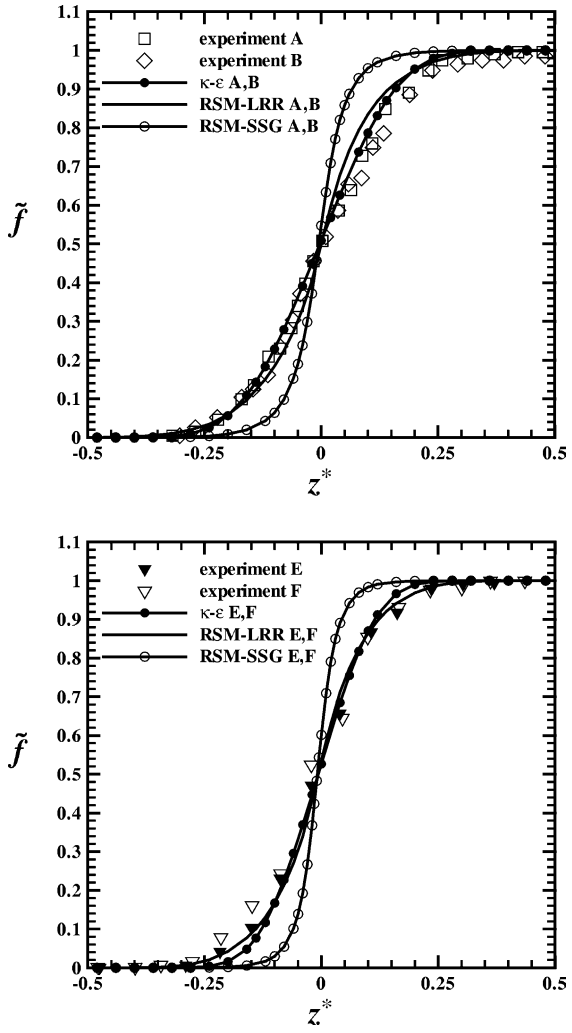


Fig. 4. Comparison of mean mixture fraction profiles showing no influence of bulk velocity. Experimental data: Mastorakos [4] (top) and Sardi et al. [32] (bottom).

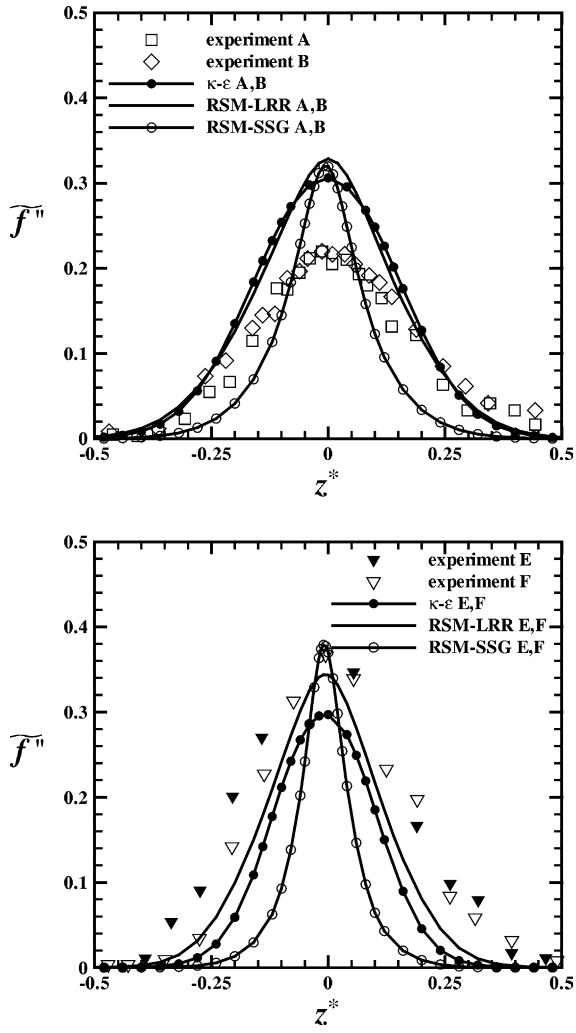


Fig. 5. Comparison of mixture fraction fluctuation profiles showing no influence of bulk velocity. Experimental data: Mastorakos [4] (top) and Sardi et al. [32] (bottom).

that the mean mixing field is independent of the bulk velocity.

The corresponding comparisons of mixture fraction fluctuation, $\widetilde{f''}$, are given in Fig. 5. Both the predicted and measured $\widetilde{f''}$ profiles peak near the stagnation plane. Similar to the mean scalar field, the bulk velocity has negligible effect on the scalar fluctuation. For Cases A and B, both the $\tilde{\kappa}$–$\tilde{\epsilon}$ and Reynolds stress models predict peak values of $\widetilde{f''}$ higher than the data by about 50%. This is in contrast to Cases E and F for which the differences between data and predictions are within 20%. Again the results from the RSM-SSG model show a much narrower mixing layer than the data although the predicted peak value is reasonable. The normalized $\tilde{\chi}$ profiles are compared in Fig. 6 for Cases E and F. Both the measurement and calculation indicate that the non-dimensional scalar dissipation rate is independent of the bulk velocity. The weak influence of bulk velocity on the scalar fluctuation may be due to the large separation between the much shorter mean flow residence time $\tau_f$ and the eddy turnover time $\tau_t$ (see Table 1). In comparison with the data, all three turbulence models over-predict $\tilde{\chi}$ by a large amount. These large discrepancies are indicative of the large uncertainties in both the measurement and the models; hence, further studies are warranted.

### 3.2. Effect of initial turbulence intensity

The computed mean axial velocity profiles by all the models reveal no dependence on exit turbulence intensity consistent with the experimental observation. As expected, Case B (the high turbulence case) has a higher level of $\widetilde{u''}$ than that of Case D (the low turbulence case).

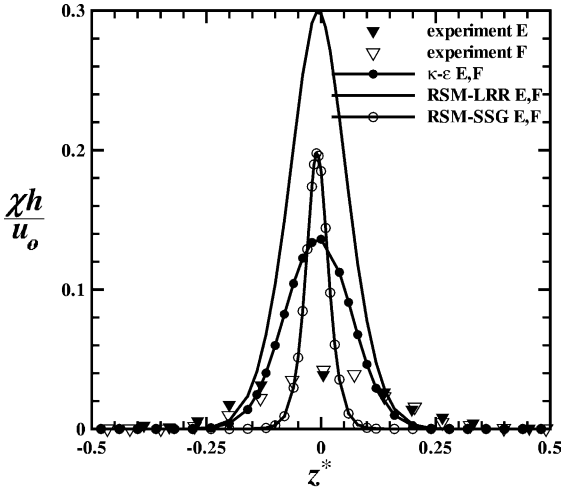


Fig. 6. Normalized scalar dissipation rate profiles predicted by various turbulence models showing no influence of bulk velocity. Experimental data: Sardi et al. [32].

The numerical results obtained with the $\tilde{\kappa}$–$\tilde{\epsilon}$ model and the RSM-LRR model give trends qualitatively consistent with the data (not shown). Comparisons of mixing field are presented in Fig. 7. Only the results of RSM-LRR model are shown for brevity. Both the measurement and the numerical results indicate that the mixing layer thickness increases with the initial turbulence intensity. The lower plot shows the profiles of $\widetilde{f''}$ and its peak value is found to increase with exit turbulence intensity. The experimentally observed effects of $C_q$ on both the peak $\widetilde{f''}$ value and the mixing layer thickness are reasonably captured by the RSM-LRR model. The $\tilde{\kappa}$–$\tilde{\epsilon}$ model (not shown) predicts the proper trend of mixing layer thickness but shows no influence of $C_q$ on the peak $\widetilde{f''}$ value.

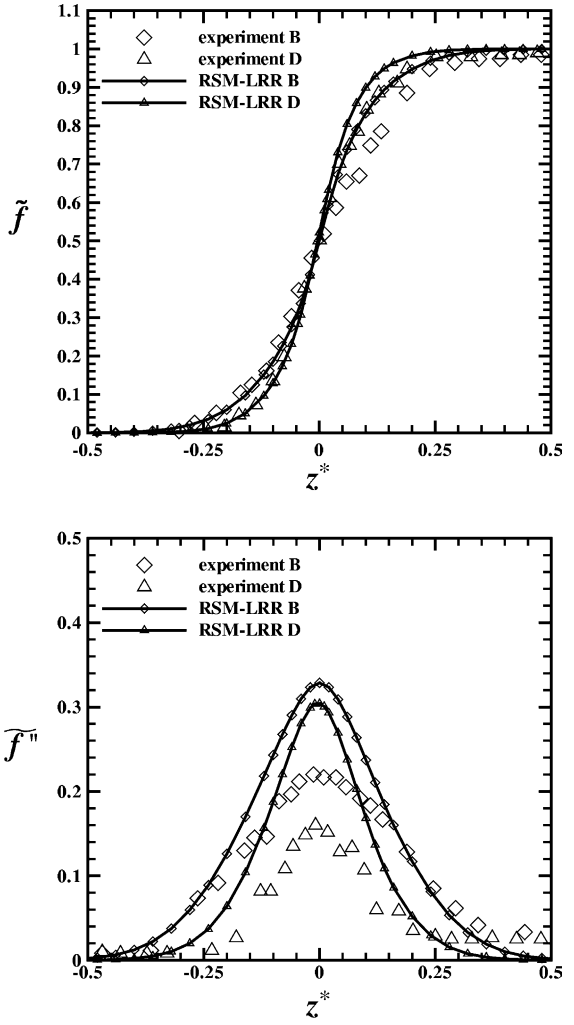


Fig. 7. Comparison of mixing field between data and predictions by LRR Reynolds stress model showing the influence of jet exit turbulence intensity. Top: mean mixture fraction; bottom: mixture fraction fluctuation; experimental data: Mastorakos [4].

### 3.3. Effect of density ratio

Both experimental and numerical results show that the mixing field of turbulent opposed-jet flows with a small density difference ($r_\rho \equiv \rho_1/\rho_0 \sim 1$) exhibits some common features. The mean axial velocity and the mean mixture fraction vary monotonically across the mixing layer and their profiles are nearly anti-symmetric with respect to the stagnation plane ($z^* = 0$). The velocity and scalar fluctuations are symmetric with respect to the stagnation plane where the fluctuations peak. To explore the effect of density variation on the mixing characteristics, Case G is conducted with a large density ratio i.e., $r_\rho = 0.14$. With Case B as a reference, Case G has the same cold (air) flow conditions as Case B but the hot air stream in Case B is replaced by a helium stream. The bulk velocity of the helium jet is increased accordingly so that both jets have the same momentum.

The predicted mean axial velocity and its fluctuation by the $\tilde{\kappa}$–$\tilde{\epsilon}$ and the RSM-LRR models are presented in Fig. 8. As seen in the figure, the predicted mean velocity profiles of Case G differ significantly from that of Case B. The mean axial velocity profiles of Case G are no longer anti-symmetric with respect to the stagnation plane. Consequently, the predicted $\widetilde{u''}$ profiles of Case G become asymmetric with respect to $z^* = 0$. Due to the

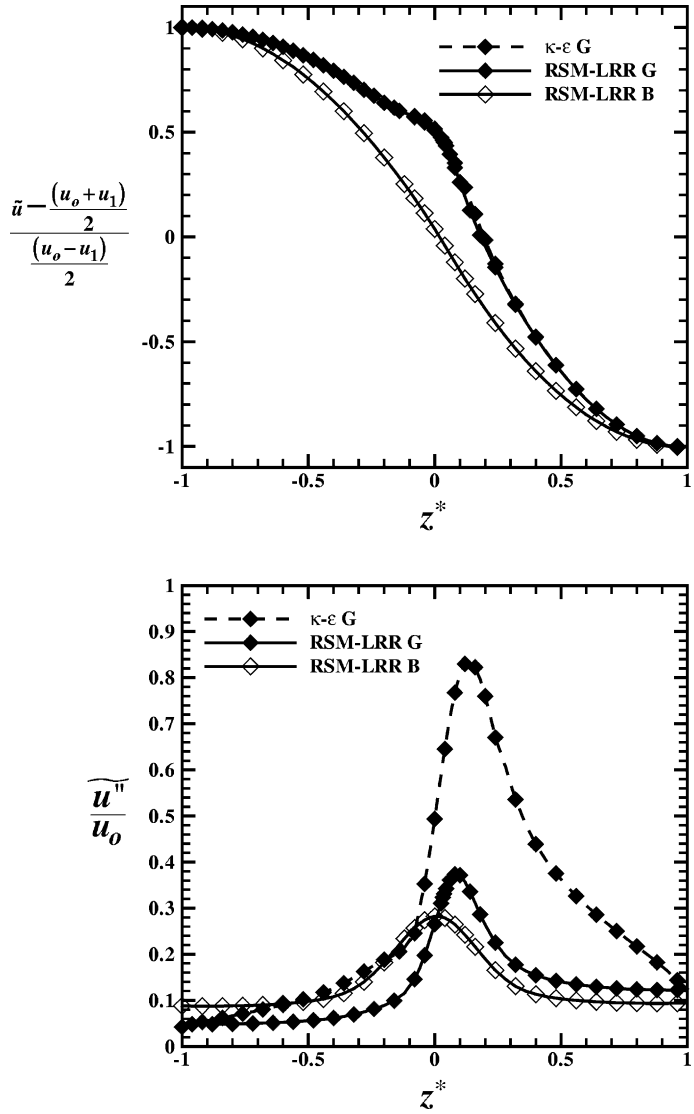


Fig. 8. Predicted velocity field of air–helium mixing by the $\tilde{\kappa}$–$\tilde{\epsilon}$ model and RSM-LRR model. Top: mean axial velocity; bottom: axial velocity fluctuation. Air side: $z^* = -1$; helium side: $z^* = 1$. Case B is provided as a reference.

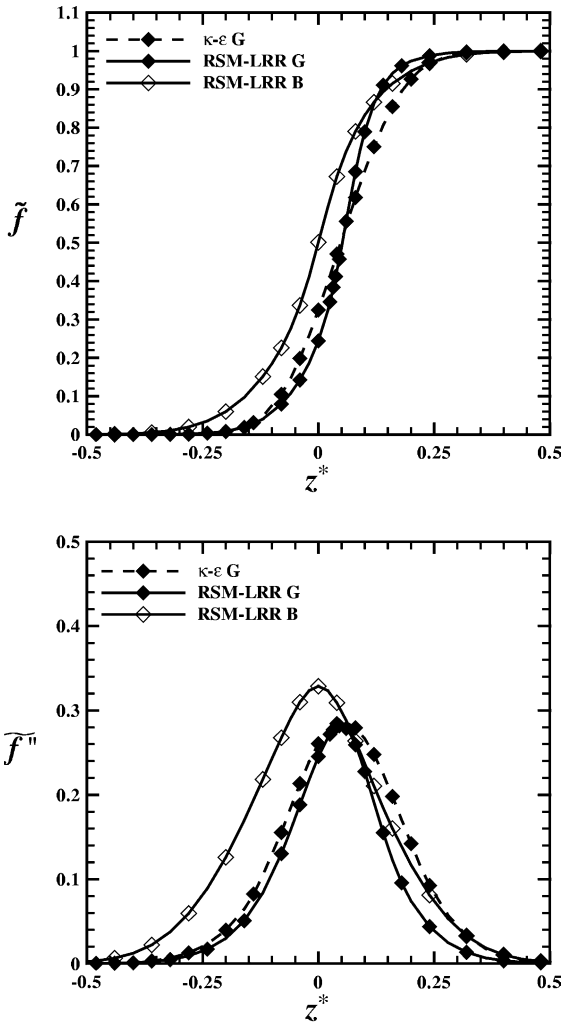


Fig. 9. Scalar mixing field of air–helium opposed jet predicted by the $\tilde{\kappa}$–$\tilde{\epsilon}$ model and RSM-LRR model. Top: mean mixture fraction; bottom: mixture fraction fluctuation.

difference in the mean velocity gradient, the turbulence production on the heavy-fluid side of the stagnation plane is smaller than that on the light-fluid side. Although the velocity field is quite different, the mean mixture fraction profile of Case G, given in Fig. 9, remains similar to cases with $r_\rho \sim 1$ except that it is shifted towards the light-fluid side. Accordingly, the predicted $\widetilde{f''}$ profiles shown in the lower plot also shift to the light-fluid side. Compared to Case B, the mixing layer of Case G is slightly narrower and the peak $\widetilde{f''}$ value is about 20% lower than that of Case B.

### 3.4. Effect of non-zero axial velocity gradient

As noted earlier, the computed mean axial velocity with the zero gradient boundary condition deviates from the measurements. It is plausible that the assumption of zero axial gradient at the nozzle exit is invalid due to the influence of an opposing jet. To assess the impact of non-zero velocity gradients on the computed results, an exploration run with conditions of Case B is repeated using the RSM-LRR model and non-zero axial velocity boundary conditions. The boundary values of the axial velocity and its gradient at the hot air jet exit are adjusted to match the measured axial velocities in regions near the jet nozzle exits. The velocity boundary conditions at the cold-air side are determined by the equal-momentum relation $\tilde{u}_{0,\mathrm{act}} = \sqrt{\bar{\rho}_1/\bar{\rho}_0}\tilde{u}_{1,\mathrm{act}}$ and by the mass conservation of the cold jet $r^2\tilde{u}_0 = r^2\tilde{u}_{0,\mathrm{act}} + 2r\tilde{v}_{0,\mathrm{act}}$, where the subscript *act* denotes the 'actual' value in distinction from the zero gradient value. These two relations lead to the specification of exit radial velocity as

$$\tilde{v}_{0,\mathrm{act}} = -r\left(\frac{\mathrm{d}\tilde{u}}{\mathrm{d}z}\right)_{0,\mathrm{act}} = \frac{r}{2}\left(\tilde{u}_0 - \tilde{u}_{0,\mathrm{act}}\right). \tag{13}$$

Based on this equation, the axial velocity gradients at both jet exits are negative and their absolute values are about 40% of the mean strain rate, i.e., $\mathrm{d}\tilde{u}/\mathrm{d}z \simeq -0.4S_\mathrm{b}$. The numerical results for the velocity and mixture fraction fields are presented in Figs. 10–12. As seen in Figs. 10 and 12, the agreements between the predicted mean values denoted by $\mathrm{d}u/\mathrm{d}z \neq 0$ and the experimental data are greatly improved. The corresponding predictions of $\widetilde{u''}$, $\widetilde{v''}$ (Fig. 11) and $\widetilde{f''}$ (Fig. 12) also agree better with the data than those obtained with $\mathrm{d}u/\mathrm{d}z = 0$, especially near the boundaries. This exercise demonstrates the importance of proper boundary conditions for the velocity gradient at jet exits. The accuracy of numerical predictions will be much improved if experiments provide

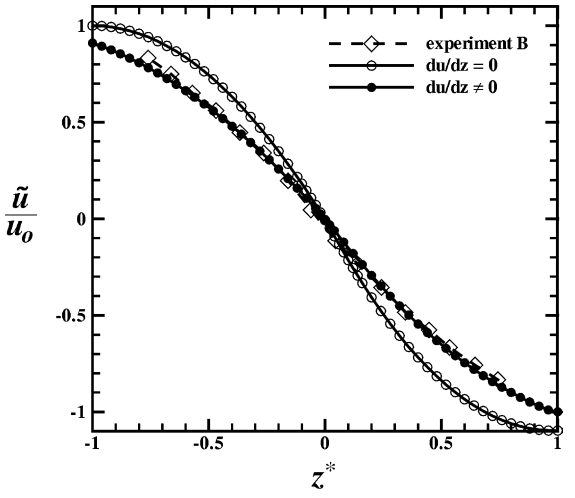


Fig. 10. Influence of non-zero axial velocity gradient boundary condition on predictions of mean axial velocity.

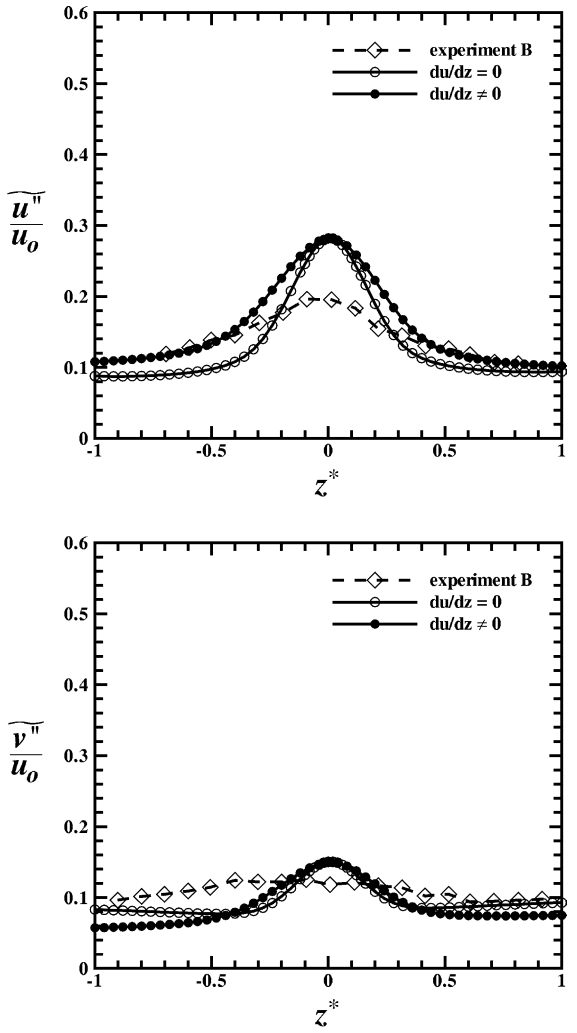


Fig. 11. Influence of non-zero axial velocity gradient boundary condition on predictions of axial (top) and radial (bottom) velocity fluctuations.

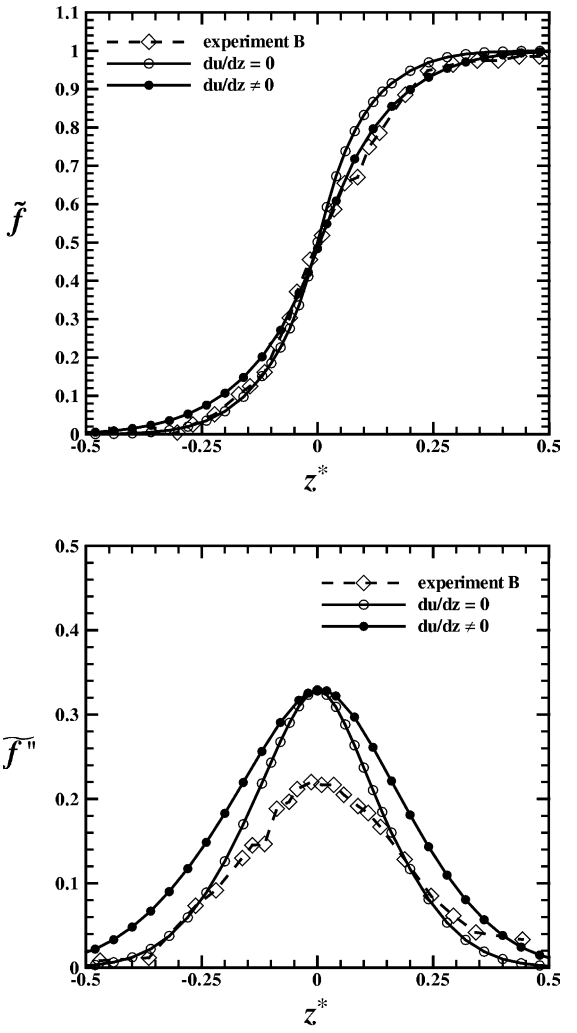


Fig. 12. Influence of non-zero axial velocity gradient boundary condition on predictions of mean mixture fraction (top) and mixture fraction fluctuations (bottom).

data on radial velocity near the jet exits. Because of the short flow residence time, the uncertainty in axial velocity gradient at the exits will not strongly affect the turbulence fields near the stagnation plan as indicated in Figs. 11 and 12. Thus the uncertainty in the boundary conditions will not alter the conclusion that the standard $\tilde{\kappa}$–$\tilde{\epsilon}$ model over-predicts the turbulent kinetic energy production as many other researchers observed in various types of stagnating flows [22,23].

### 3.5. Mechanical-to-scalar time scale ratio

With the results from the RSM-LRR model, the $C_D$ distributions for five different cases are deduced and plotted in Fig. 13. Outside the mixing layer $C_D$ is zero and its value rises sharply near the edges of the mixing layer. At the stagnation plane, $C_D$ reaches its peak value. For cases with small density differences, the computed $C_D$ profiles are found to depend on both the initial turbulence intensity and the ratio of the flow residence time to the large-eddy turnover time ($\tau_f/\tau_t$). The $C_D$ level is found to be high when the value of either $C_q$ or $\tau_f/\tau_t$ is low. As listed in Table 1, Case D has the lowest values for both $C_q$ and $\tau_f/\tau_t$ among the four cases (A, B, D, E). The corresponding $C_D$ value is the highest among the cases. Since both Case A and Case B have identical $C_D$ profiles, the bulk velocity has no effect on the computed $C_D$ level. Because of the relatively 'young' turbulence (small $\tau_f/\tau_t$), the $C_D$ levels of Cases A, B and D are greater than 3. The peak $C_D$ value of Case G is seen comparable with those of Cases A and B. However, the $C_D$ level of Case G is low on the heavy-fluid side of

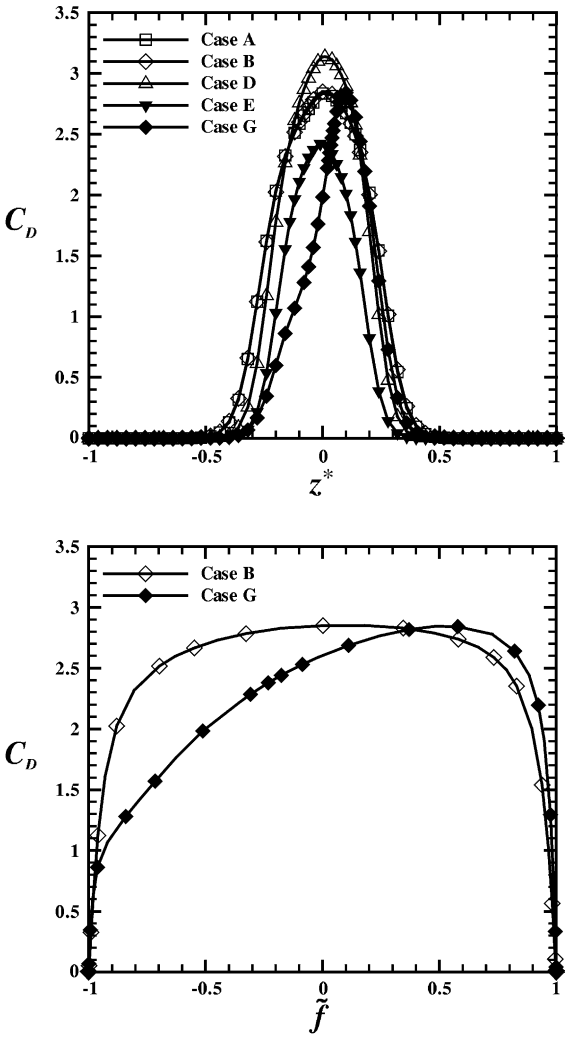


Fig. 13. Distributions of mechanical-to-scalar time scale ratio predicted by the second-order scalar (RSM-LRR) model for constant density mixing Cases A, B, D, and E as well as variable density mixing Case G listed in Table 1.

mixing layer. In the lower plot, the effect of density variation on $C_D$ is plotted versus mixture fraction showing a larger variation when the density difference increases. Therefore, the practice of assigning a constant value for $C_D$ is questionable for modeling flows with large density changes.

## 4. Conclusion

A study of turbulent opposed-jet flows using 1-D formulation with both the $\tilde{\kappa}$–$\tilde{\epsilon}$ and Reynolds stress models is reported with extensive comparisons with experimental data. Both data and numerical results using Reynolds stress models show that the turbulence is highly anisotropic. Among the three turbulence models studied, the combination of the RSM-LRR model and the second-order scalar model gives the most satisfactory predictions. The numerical model confirms that both the velocity and the scalar fields are not affected by the bulk velocity in accord with the experimental observation. Model predictions of the influence of jet exit turbulence intensity on the velocity and scalar field are found satisfactory. Model results reveals that the jet density ratio has strong influence on the characteristics of both the velocity and scalar fields. An exploration study demonstrates that the importance of proper specification of axial velocity gradient. The time scale ratio between the turbulence and the scalar fields is deduced from computed results. Its value is found nearly constant inside the mixing layer ranging from 2.5 to 3.0. Density variation is shown to affect the time scale ratio noticeably implying that using a fixed value may be inadequate for opposed-jet flows with large density variations.

## Appendix A. Reynolds stress closure

Two versions of Reynolds stress closure are considered: one was proposed by Launder et al. (RSM-LRR) [19] and the other by Speziale et al. (RSM-SSG) [20]. The major difference between these two models lies in the modeling of the pressure–strain correlations. In RSM-LRR, the coefficients of the rapid part of the pressure–strain correlation are linear functions of the anisotropy tensor while the coefficients in RSM-SSG are quadratically non-linear. The transport equations of $\widetilde{u''u''}$, $\widetilde{v''v''}$, and $\widetilde{u''v''}/r$ are listed in sequence

$$2U\frac{\mathrm{d}\tau_{uu}}{\mathrm{d}z}=\frac{\mathrm{d}}{\mathrm{d}z}\left(\bar{\rho}C_s\tau_{uu}\frac{\tilde{\kappa}}{\tilde{\epsilon}}\frac{\mathrm{d}\tau_{uu}}{\mathrm{d}z}\right)+\bar{\rho}C_s\tau_{uv}\frac{\tilde{\kappa}}{\tilde{\epsilon}}\frac{\mathrm{d}\tau_{uu}}{\mathrm{d}z}+\bar{\rho}\widehat{P}_{uu}+\bar{\rho}\pi_{uu}-\frac{2}{3}\bar{\rho}\tilde{\epsilon}, \tag{A.1}$$

$$2U\frac{\mathrm{d}\tau_{vv}}{\mathrm{d}z}=\frac{\mathrm{d}}{\mathrm{d}z}\left(\bar{\rho}C_s\tau_{uu}\frac{\tilde{\kappa}}{\tilde{\epsilon}}\frac{\mathrm{d}\tau_{vv}}{\mathrm{d}z}\right)+\bar{\rho}C_s\tau_{uv}\frac{\tilde{\kappa}}{\tilde{\epsilon}}\frac{\mathrm{d}\tau_{vv}}{\mathrm{d}z}+\bar{\rho}\widehat{P}_{vv}+\bar{\rho}\pi_{vv}-\frac{2}{3}\bar{\rho}\tilde{\epsilon}, \tag{A.2}$$

$$2U\frac{\mathrm{d}\tau_{uv}}{\mathrm{d}z}-G\tau_{uv}=\frac{\mathrm{d}}{\mathrm{d}z}\left[\bar{\rho}C_s\frac{\tilde{\kappa}}{\tilde{\epsilon}}\left(\tau_{uu}\frac{\mathrm{d}\tau_{uv}}{\mathrm{d}z}+\tau_{uv}^2\right)\right]+2\bar{\rho}C_s\tau_{uv}\frac{\tilde{\kappa}}{\tilde{\epsilon}}\frac{\mathrm{d}\tau_{uv}}{\mathrm{d}z}+\bar{\rho}\frac{\widehat{P}_{uv}}{r}+\bar{\rho}\frac{\pi_{uv}}{r}. \tag{A.3}$$

The turbulence production is evaluated by the individual Reynolds stress component as

$$\widehat{P}_{uu} = -4\tau_{uu}\frac{\mathrm{d}}{\mathrm{d}z}\left(\frac{U}{\bar{\rho}}\right), \quad \widehat{P}_{vv} = 2\tau_{vv}\frac{G}{\bar{\rho}},$$

$$\frac{\widehat{P}_{uv}}{r} = \tau_{uu}\frac{\mathrm{d}}{\mathrm{d}z}\left(\frac{G}{\bar{\rho}}\right) + \tau_{uv}\left[-2\frac{\mathrm{d}}{\mathrm{d}z}\left(\frac{U}{\bar{\rho}}\right) + \frac{G}{\bar{\rho}}\right].$$

The pressure–strain correlations, i.e., $\pi_{uu}$, $\pi_{vv}$, and $\pi_{uv}$, are given in [7]. By including the anisotropic effects, the $\tilde{\epsilon}$ equation for the RSM becomes

$$2U\frac{\mathrm{d}\tilde{\epsilon}}{\mathrm{d}z} = \frac{\mathrm{d}}{\mathrm{d}z}\left(\bar{\rho}C_{s\epsilon}\tau_{uu}\frac{\tilde{\kappa}}{\tilde{\epsilon}}\frac{\mathrm{d}\tilde{\epsilon}}{\mathrm{d}z}\right) + \bar{\rho}C_{s\epsilon}\tau_{uv}\frac{\tilde{\kappa}}{\tilde{\epsilon}}\frac{\mathrm{d}\tilde{\epsilon}}{\mathrm{d}z} + C_{\epsilon 1}\bar{\rho}\frac{\tilde{\epsilon}}{\tilde{\kappa}}\widehat{P} - C_{\epsilon 2}\bar{\rho}\frac{\tilde{\epsilon}^2}{\tilde{\kappa}}, \tag{A.4}$$

where $C_{s\epsilon} = 0.15$, $C_{\epsilon 1} = 1.44$, $C_{\epsilon 2} = 1.92$ for RSM-LRR and $C_{s\epsilon} = 0.15$, $C_{\epsilon 1} = 1.44$, $C_{\epsilon 2} = 1.83$ for RSM-SSG. Boundary values of the Reynolds stress components are estimated by assuming isotropic turbulence at the jet exits as $\tau_{uu}(0) = \tau_{vv}(0) = \tau_{ww}(0) = 2\tilde{\kappa}(0)/3$, $\tau_{uu}(h) = \tau_{vv}(h) = \tau_{ww}(h) = 2\tilde{\kappa}(h)/3$, and $\tau_{uv}(0) = \tau_{uv}(h) = 0$.

## References


[1] C.K. Law, D.L. Zhu, G. Yu, Propagation and extinction of stretched premixed flames, in: Proceedings of the Combustion Institute, vol. 21, The Combustion Institute, 1986, pp. 1419–1426.

[2] R.J. Kee, J.A. Miller, G.H. Evans, G. Dixon-Lewis, A computational model of the structure and extinction of strained, opposed flow, premixed methane–air flames, in: Proceedings of the Combustion Institute, vol. 22, The Combustion Institute, 1988, pp. 1479–1494.

[3] M. Nishioka, S. Nakagawa, Y. Ishikawa, T. Takeno, NO emission characteristics of methane–air double flame, Combust. Flame 98 (1994) 127–138.

[4] E. Mastorakos, Turbulent combustion in opposed jet flows, Ph.D. thesis, Imperial College of Science, Technology, and Medicine, London, UK, 1993.

[5] L.W. Kostiuk, K.N.C. Bray, T.C. Chew, Premixed turbulent combustion in counterflowing streams, Combust. Sci. Technol. 64 (1989) 233–241.

[6] L.W. Kostiuk, P.A. Libby, Comparison between theory and experiment for turbulence in opposed streams, Phys. Fluids A 5 (9) (1993) 2301–2303.

[7] C.-P. Chou, J.-Y. Chen, J. Janicka, E. Mastorakos, One-dimensional description of turbulent opposed-jet flows with $\tilde{\kappa}$–$\tilde{\epsilon}$ model and second-order closure, in: The 2nd Joint Meeting of The U.S. Sections of The Combustion Institute, Paper No. 180, Oakland, CA, March 25–28, 2001.

[8] K.N.C. Bray, M. Champion, P.A. Libby, Premixed flames in stagnating turbulence. Part I. The general formulation for counterflowing streams and gradient models for turbulent transport, Combust. Flame 84 (1991) 391–410.

[9] K.N.C. Bray, M. Champion, P.A. Libby, Premixed flames in stagnating turbulence. Part III. The $\tilde{\kappa}$–$\tilde{\epsilon}$ theory for reactants impinging on a wall, Combust. Flame 91 (1992) 165–186.

[10] K.N.C. Bray, M. Champion, P.A. Libby, Premixed flames in stagnating turbulence. Part II. The mean velocities and pressure and Damköhler number, Combust. Flame 112 (1998) 635–654.

[11] K.N.C. Bray, M. Champion, P.A. Libby, Premixed flames in stagnating turbulence. Part IV. A new theory for the Reynolds stresses and Reynolds fluxes applied to impinging flows, Combust. Flame 120 (2000) 1–18.

[12] F.A. Maury, P.A. Libby, Nonpremixed flames in stagnating turbulence. Part I. The $\tilde{\kappa}$–$\tilde{\epsilon}$ theory with equilibrium chemistry for the methane–air system, Combust. Flame 102 (1995) 341–356.

[13] M. Champion, P.A. Libby, Reynolds stress description of opposed and impinging turbulent jets. Part I. Closely spaced opposed jets, Phys. Fluids A 5 (1) (1993) 203–216.

[14] M. Champion, P.A. Libby, Reynolds stress description of opposed and impinging turbulent jets. II. Axisymmetric jets impinging on nearby walls, Phys. Fluids 6 (5) (1994) 1805–1819.

[15] W.P. Jones, Y. Prasetyo, Probability density function modeling of premixed turbulent opposed jet flames, in: Proceedings of the Combustion Institute, vol. 26, The Combustion Institute, 1996, pp. 275–282.

[16] R.P. Lindstedt, E.M. Vãos, Modeling of premixed turbulent flames with second moment methods, Combust. Flame 116 (1999) 461–485.

[17] S.C. Li, P.A. Libby, F.A. Williams, Experimental investigation of a premixed flame in an impinging turbulent stream, in: Proceedings of the Combustion Institute, vol. 25, The Combustion Institute, 1994, pp. 1207–1214.

[18] W.P. Jones, J.H. Whitelaw, Calculation methods for reacting turbulent flows: a review, Combust. Flame 48 (1982) 1–26.

[19] B.E. Launder, G.J. Reece, W. Rodi, Progress in the development of a Reynolds-stress turbulence closure, J. Fluid Mech. 68 (1975) 537–566.

[20] C.G. Speziale, S. Sarkar, T.B. Gatski, Modelling the pressure–strain correlation of turbulence: an invariant dynamical systems approach, J. Fluid Mech. 227 (1991) 245–272.

[21] K. Seshadri, F.A. Williams, Laminar flow between parallel plates with injection of a reactant at high Reynolds number, Int. J. Heat Mass Transfer 21 (1978) 251–253.

[22] D.B. Taublee, L. Tran, Stagnating streamline turbulence, AIAA J. 26 (8) (1988) 1011–1013.

[23] P.A. Durbin, On the k-3 stagnation point anomaly, Int. J. Heat Fluid Flow 17 (1996) 89–90.

[24] P.A. Durbin, Separated flow computations with the $\kappa$–$\epsilon$–$v^2$ model, AIAA J. 33 (4) (1995) 659–664.

[25] S.E. Elghobashi, B.E. Launder, Turbulent time scales and the dissipation rate of temperature variance in the thermal mixing layer, Phys. Fluids 26 (9) (1983) 2415–2419.

[26] W.P. Jones, P. Musonge, Closure of the Reynolds stress and scalar flux equations, Phys. Fluids 31 (12) (1988) 3589–3604.

[27] C. Béguier, I. Dekeyser, B.E. Launder, Ratio of scalar and velocity dissipation time scales in shear flow turbulence, Phys. Fluids 21 (3) (1978) 307–310.

[28] Z. Warhaft, J.L. Lumley, An experimental study of the decay of temperature fluctuations in grid-generated turbulence, J. Fluid Mech. 88 (1978) 659–684.
[29] V. Eswaran, S.B. Pope, Direct numerical simulations of the turbulent mixing of a passive scalar, Phys. Fluids 31 (3) (1988) 506–520.
[30] G.R. Newman, B.E. Launder, J.L. Lumley, Modelling the behaviour of homogeneous scalar turbulence, J. Fluid Mech. 111 (1981) 217–232.
[31] E. Mastorakos, A.M.K.P. Taylor, J.H. Whitelaw, Mixing in turbulent opposed jet flows, in: F. Durst et al. (Eds.), Turbulent Shear Flows 9, Springer-Verlag, New York, 1994, pp. 149–166.
[32] K. Sardi, A.M.K.P. Taylor, J.H. Whitelaw, Conditional scalar dissipation statistics in a turbulent counterflow, J. Fluid Mech. 361 (1998) 1–24.